



ELSEVIER

Available online at www.sciencedirect.com

SCIENCE @ DIRECT®

Ocean Modelling 6 (2004) 51–81

**Ocean
Modelling**

www.elsevier.com/locate/omodel

Non-uniform adaptive vertical grids in one-dimensional numerical ocean models

Hans Burchard ^{a,*}, Jean-Marie Beckers ^b

^a *Baltic Sea Research Institute Warnemünde, Seestr. 15, D-18119 Rostock-Warnemünde, Germany*

^b *MARE-GHER-AGO, University of Liège, Sart-Tilman B5, B-4000 Liège, Belgium*

Received 6 September 2002; received in revised form 13 November 2002; accepted 13 November 2002

Abstract

It is demonstrated in this paper how the concept of general vertical coordinates can be exploited for constructing adaptive grids in primitive equation ocean models. The term *adaptive* is used here in the sense of coordinate iso-surfaces which follow certain internal structures of the flow in such a way that higher vertical resolution is obtained in locations where vertical gradients are large. The internal structures considered here are shear and stratification. In this paper, one-dimensional models are applied in order to demonstrate the ability of such grid adaptation methods to follow internal structures even in flow situations dominated by vertical mixing processes. Here, a variational approach is considered for the generation of grids which results in a diffusion equation for the vertical coordinate. The method is tested for five different idealised and realistic scenarios with the result that the discretisation error can be significantly reduced in comparison to equidistant Cartesian grids. Some recommendations for extending these methods for three-dimensional models are given at the end of this paper.

© 2003 Elsevier Science Ltd. All rights reserved.

1. Introduction

Until a few years ago, numerical ocean models based on primitive equations could be classified in terms of vertical discretisations as being basically z -coordinate models, σ -coordinate models or isopycnal models.

The archetype of z -coordinate models is the well-known MOM (Modular Ocean Model, see Bryan, 1969) in which a straightforward discretisation in the Cartesian coordinates with stepwise

* Corresponding author.

E-mail addresses: hans.burchard@io-warnemuende.de (H. Burchard), jm.beckers@ulg.ac.be (J.-M. Beckers).

representation of topography is used. A classical σ -coordinate model is POM (Princeton Ocean Model, Blumberg and Mellor, 1987), in which each water column is subdivided into a constant number of vertical levels, the relative distribution of which remains fixed. The typical example for isopycnal models is MICOM (Miami Isopycnal Coordinate Ocean Model, Bleck et al., 1992) in which the vertical coordinate is chosen such that in each numerical layer the density is constant. Each of these model types has its own advantages and disadvantages which were extensively discussed by Griffies et al. (2000).

Most currently used models fall in one of these categories of models (see the textbook by Haidvogel and Beckmann (1999)), though some hybridisations and adaptations were performed in order to increase accuracy or eliminate drawbacks. Masked and generalised σ -coordinate models (see Beckers, 1991; Gerdes, 1993), were used to reduce problems associated with pressure gradient errors. Some adaptations to isopycnal models allow a transition to level (z) coordinates near the ocean surface to provide vertical resolution in the mixed layer (Bleck, 2002) in order to better represent mixing effects. z -coordinate models have also been adapted to include for example improved down-slope flow over z -coordinate model steps (see Beckmann and Döscher, 1997) or to include real topography instead of stepwise topography (see Griffies et al., 2000). Those and other adaptations primarily represent modifications in the primary vertical coordinate system in each of these model types.

It is somehow surprising that only very recently generalised vertical coordinate transformations (already introduced much earlier by Kasahara (1974)) started to be implemented into ocean models. The so-called s -coordinate models or hybrid coordinate models (see Song and Haidvogel, 1994; Burchard and Petersen, 1997; Madec et al., 1998; Pietrzak et al., 2002) are now becoming new standard modelling tools. They allow vertical coordinates to be located in a completely arbitrary way. Presently the practical use of these generalised coordinates is however limited by the fact that there is no clear strategy to construct the coordinates in an optimal way. Typically these hybrid models are used in an “a priori” way, where the coordinates are placed according to the modellers a priori knowledge of the processes to be properly resolved. This approach is certainly already advantageous compared to the classic models where such a free choice is not possible, but it does not use the possibility of adapting the coordinate positions during the calculation according to the modelling results themselves.¹ Though standard in classic computational fluid dynamics (see Thompson et al., 1985; Liseikin, 1999) or atmospheric models (see Fiedler, 2002), the use of adaptive vertical grids in ocean models is rare. Exceptions are the use of grid adaptation by empirical functions to achieve boundary layer refinements in isopycnal models (see Dewar and McDougall, 2000; Holt and James, 2001; Bleck, 2002).

However there is no general strategy which allows the design of grid refinements on a rational minimisation of expected model errors. Therefore we will introduce in the present paper a method based on a priori minimisations of global errors (see Thompson et al., 1985). This variational approach leads to Euler–Lagrange equations which can be iteratively solved by a time-stepping method. Therefore, this approach is very easily incorporated into the time evolution of the model,

¹ σ -coordinate models are of course adaptive grids in the sense that they follow sea surface elevation changes, and isopycnal models are also adaptive in the sense that they follow isopycnals. Here we refer to adaptive grids as to those which explicitly include a strategy to modify the vertical distributions of coordinate points by other means.

simply by iterating during the model time steps. The approach is also very easily incorporated into three-dimensional models, in contrast to algebraic gridding techniques which generally ask for direct generation of full three-dimensional grids rather than iterative modifications. We therefore prefer the approach based on successive modifications of an existing grid in order to be able to include it easily in a three-dimensional model.

Here we will concentrate on a one-dimensional model version in order to verify if the approach performs correctly in cases where vertical mixing is the most important process, keeping in mind the need for later generalisations to three-dimensional versions and the processes that could be important to take into account in a numerically sound way in the three-dimensional case (like isopycnal diffusion, see Beckers et al. (2000), pressure gradient errors, see Deleersnijder and Ruddick (1992), downslope flows, see Beckmann and Döscher (1997) internal waves, see Stanev and Beckers (1999)) when adapting the grids.

The paper is organised as follows: First the concept of general vertical coordinates is briefly reviewed with respect to the one-dimensional idealisation of the primitive equations (Section 2). Then, the grid adaptation strategy is derived from the variational approach and described in detail (Section 3). Afterwards, the numerical methods for solving the dynamical equations in the framework of the moving grids are discussed (Section 4). These methods are then compared and investigated in detail for five different idealised and realistic model scenarios (Sections 5.1–5.5). Finally, the results are summarised and discussed, and perspectives for extensions to three-dimensional models are discussed (Section 6).

2. General vertical coordinates

The coordinates that span the Cartesian space will be denoted as (t^*, x^*, y^*, z) , derivatives along these coordinates will be marked by asterisks. The one-dimensional primitive equations for modelling geophysical ocean and coastal dynamics read in these coordinates as

$$\partial_t^* u - \partial_z^*(v_t \partial_z^* u) - fv = -g \partial_x^* \zeta, \quad (1)$$

$$\partial_t^* v - \partial_z^*(v_t \partial_z^* v) + fu = -g \partial_y^* \zeta, \quad (2)$$

$$\partial_t^* T - \partial_z^*(v_t' \partial_z^* T) = \frac{\partial_z^* I}{c_p' \rho_0}, \quad (3)$$

$$\partial_t^* S - \partial_z^*(v_t' \partial_z^* S) = 0. \quad (4)$$

Here, u , v , T and S are the velocity components with respect to the x - and y -directions, the potential temperature and salinity, respectively. The vertical coordinate z ranges from the bottom at $z = -H$ to the surface at $z = \zeta$. v_t is the vertical eddy viscosity; v_t' , the vertical eddy diffusivity; g , the gravitational acceleration, and f , the Coriolis parameter. The surface elevation slopes $\partial_x^* \zeta$ and $\partial_y^* \zeta$ have to be prescribed in this one-dimensional model framework, internal pressure gradients are not considered here, although it would be possible also in one-dimensional models (see Simpson et al., 2002). Potential density ρ is calculated by the equation of state,

$$\rho = \rho(T, S, p_0), \quad (5)$$

which is here calculated by means of the UNESCO equation, see Gill (1982), with p_0 denoting surface pressure. For idealised scenarios, a dynamic equation for the buoyancy

$$b = -g \frac{\rho - \rho_0}{\rho_0}, \quad (6)$$

with the constant reference density ρ_0 is often preferred for simplicity:

$$\partial_t^* b - \partial_z^* (v_t' \partial_z^* b) = 0. \quad (7)$$

The vertical mixing coefficients v_t for momentum and v_t' for tracers are calculated by means of a two-equation turbulence model which is here a k - ε model adopted from Burchard and Bolding (2001) with the turbulent kinetic energy (TKE), k , and the dissipation rate of the TKE, ε . The two prognostic equations for k and ε read:

$$\partial_t^* k - \partial_z^* \left(\frac{v_t}{\sigma_k} \partial_z^* k \right) = P + B - \varepsilon, \quad (8)$$

$$\partial_t^* \varepsilon - \partial_z^* \left(\frac{v_t}{\sigma_\varepsilon} \partial_z^* \varepsilon \right) = \frac{\varepsilon}{k} (c_{1\varepsilon} P + c_{3\varepsilon} B - c_{2\varepsilon} \varepsilon). \quad (9)$$

In (8) and (9),

$$P = v_t M^2; \quad B = -v_t' N^2 \quad (10)$$

with

$$M^2 = (\partial_z^* u)^2 + (\partial_z^* v)^2; \quad N^2 = \partial_z^* b \quad (11)$$

are shear and buoyancy production, respectively, and σ_k , σ_ε , $c_{1\varepsilon}$, $c_{2\varepsilon}$ and $c_{3\varepsilon}$ are empirical constants. By means of an algebraic second moment closure of the Reynolds-averaged Navier–Stokes equations, it can be shown that the following relations hold for the eddy viscosity and diffusivity (see Burchard and Bolding, 2001):

$$v_t = c_\mu \frac{k^2}{\varepsilon}, \quad v_t' = c'_\mu \frac{k^2}{\varepsilon} \quad (12)$$

with the non-dimensional so-called stability functions

$$c_\mu = c_\mu(\alpha_M, \alpha_N), \quad c'_\mu = c'_\mu(\alpha_M, \alpha_N) \quad (13)$$

and

$$\alpha_M = M^2 \frac{k^2}{\varepsilon^2}, \quad \alpha_N = N^2 \frac{k^2}{\varepsilon^2}. \quad (14)$$

The actual structure of the stability functions depends on details of the second moment closure. Here, the closure by Canuto et al. (2001) has been used, see also Burchard and Bolding (2001).

It should be emphasised that the shear frequency squared, M^2 , and the Brunt–Väisälä frequency squared, N^2 , play a major role in the parameterisation of the vertical mixing. Thus, these two will be the major parameters for computing the adaptive grids, see Section 3.

For all dynamical equations, surface and bottom boundary conditions have to be provided. At the surface, the boundary fluxes for u , v , T , and S are taken from idealised assumptions or

meteorological observations, at the bottom the law of the wall with zero fluxes for T and S is assumed. For k and ε , the law of the wall is used at the bottom and the surface, where wave-breaking phenomena are not considered.

In order to increase the mathematical flexibility of the model, a general vertical coordinate transformation following Kasahara (1974) and Deleersnijder and Ruddick (1992) is carried out which maps the physical space into a transformed space spanned by the coordinates (t, x, y, γ) . The general vertical coordinate γ is assumed to be monotone with respect to z :

$$\gamma = \gamma(t^*, x^*, y^*, z) \iff z = z(t, x, y, \gamma). \quad (15)$$

Derivatives in the transformed space will be denoted by ∂_t , ∂_x , ∂_y and ∂_γ . The values for γ at the bottom and the surface are constant in time and space so that the approach shown here provides boundary fitted coordinates in the vertical. Here,

$$\gamma(\zeta) = 0, \quad \gamma(-H) = -1 \quad (16)$$

are used. The so-called Jacobian of the transformation,

$$J := \partial_\gamma z = (\partial_z^* \gamma)^{-1}, \quad (17)$$

plays a central role in the transformation of the equations. With these definitions, the dynamic equations for u , v , T , S , k and ε read:

$$\partial_t(Ju) + \partial_\gamma(\tilde{w}u) - \partial_\gamma\left(\frac{v_t}{J}\partial_\gamma u\right) - fJv = -Jg\partial_x^*\zeta, \quad (18)$$

$$\partial_t(Jv) + \partial_\gamma(\tilde{w}v) - \partial_\gamma\left(\frac{v_t}{J}\partial_\gamma v\right) + fJu = -Jg\partial_y^*\zeta, \quad (19)$$

$$\partial_t(JT) + \partial_\gamma(\tilde{w}T) - \partial_\gamma\left(\frac{v_t'}{J}\partial_\gamma T\right) = J\frac{\partial_z^* I}{c_p' \rho_0}, \quad (20)$$

$$\partial_t(JS) + \partial_\gamma(\tilde{w}S) - \partial_\gamma\left(\frac{v_t'}{J}\partial_\gamma S\right) = 0, \quad (21)$$

$$\partial_t(Jk) + \partial_\gamma(\tilde{w}k) - \partial_\gamma\left(\frac{v_t}{J\sigma_k}\partial_\gamma k\right) = J(P + B - \varepsilon), \quad (22)$$

$$\partial_t(J\varepsilon) + \partial_\gamma(\tilde{w}\varepsilon) - \partial_\gamma\left(\frac{v_t}{J\sigma_\varepsilon}\partial_\gamma \varepsilon\right) = \frac{J\varepsilon}{k}(c_{1\varepsilon}P + c_{3\varepsilon}B - c_{2\varepsilon}\varepsilon). \quad (23)$$

Here,

$$\tilde{w} = J\partial_t^* \gamma = -\partial_t z \quad (24)$$

is the vertical velocity relative to the grid transformation. Thus, an upward motion of the grid at a velocity of $\partial_t z$ is compensated by a downward advective velocity (relative to the moving grid) of \tilde{w} and vice versa. In three-dimensional models, where a physical vertical velocity component is generally present, the grid related vertical velocity is composed of the physical vertical velocity component, the negative grid velocity, and terms related to the slope of the grid lines. For more details of the transformation, see e.g. Burchard and Petersen (1997).

3. Adaptive grid generation strategies

The most simple coordinate transformation in this concept is the σ -coordinate with

$$\gamma = \sigma = \frac{z - \zeta}{D}, \quad (25)$$

with $J = D = \zeta + H$, first introduced to the modelling of natural waters by Freeman et al. (1992). Other, more complex coordinates are the near-bed transformation by de Kok (1992), the s -coordinate by Song and Haidvogel (1994) or the mixed-layer transformation by Burchard and Petersen (1997) (see also Burchard and Bolding, 2002). In contrast to these transformations which do only depend on the bottom topography and the sea surface elevation (i.e. barotropic features) we introduce here baroclinic transformations which adapt to the internal dynamics of the flow.

Our choice is based on the cost function \mathcal{J} defined by

$$\mathcal{J}_1 = \int_{-h}^{\zeta} (\partial_{\sigma} f) dz = \int_{-1}^0 \partial_z f (\partial_{\sigma} z)^2 d\sigma = \int_{-1}^0 w_1 (\partial_{\sigma} z)^2 d\sigma \quad (26)$$

Here the weight $w_1 = f'$ is obviously related to the rate of change of the function f or alternatively to the inverse length scale of the function variations ($'$ stands for a derivative with respect to the physical coordinate z).

Minimisation of (26) tries to find the coordinate change $z = z(\sigma)$ such that in the new coordinates, the gradients (with respect to the new coordinate) of f are uniform and small, a feature which should simplify numerical representations of the function.

The Euler–Lagrange equation for fixed end points $z(-1) = -H$ and $z(0) = \zeta$ and assuming the weighting function depending on the normalised coordinates: $w_1 = w_1(\sigma)$ reads then

$$\partial_{\sigma}(w_1 \partial_{\sigma} z) = 0. \quad (27)$$

However, in practise the weighting will be dependent on physical space coordinates since ultimately this is what is of interest to the modeller. This can be handled by using Eq. (27) with a diffusion term for a discrete set of σ levels, but where w_1 must be updated at each change of z . It means that (27) is essentially non-linear in that case. Another approach would be to accept the a priori dependence of w_1 on the physical space and to minimise instead

$$\mathcal{J}_2 = \int_{-1}^0 (w_1(z) \partial_{\sigma} z)^2 d\sigma \quad (28)$$

which leads to the same Euler–Lagrange equation as (27).

It can easily be shown that this approach minimises the error when assuming piecewise constant functions for a discrete set of data points. Indeed the truncation error T_1 of such an “interpolation” technique is roughly

$$T_1 = \hat{\partial}_{\sigma} z \hat{\partial}_z f, \quad (29)$$

so that its minimisation over the physical domain is nothing else than the minimisation of \mathcal{J}_1 .

In order to obtain this minimisation, the following diffusion equation is solved for the vertical coordinate z in the normalised z -space (or σ -space):

$$\partial_t z - \partial_\sigma (k^{\text{grid}} \partial_\sigma z) = 0 \quad (30)$$

with the grid-related diffusivity k^{grid} and $\sigma \in [-1, 0]$ and boundary conditions for z from $z(-1) = -D$ and $z(0) = \zeta$.

The grid diffusion coefficient k^{grid} (which has the physical unit s^{-1}) is calculated as:

$$k^{\text{grid}} = \frac{cD}{T^{\text{grid}}} \left(c_\rho K_\rho^{\text{grid}} + c_u K_u^{\text{grid}} + c_d K_d^{\text{grid}} + c_b K_b^{\text{grid}} \right) \quad (31)$$

with the stratification-related component

$$K_\rho^{\text{grid}} = \frac{\max(0, \partial_z \rho)}{\Delta \rho}, \quad (32)$$

the shear-related component

$$K_u^{\text{grid}} = \frac{M}{\Delta u}, \quad (33)$$

the near-surface component

$$K_d^{\text{grid}} = \frac{1}{d + d_0}, \quad (34)$$

and the background component

$$K_b^{\text{grid}} = \frac{1}{D}. \quad (35)$$

Here $\Delta \rho$ is a reference density difference and Δu , a reference velocity difference. The grid diffusion time scale is denoted by T^{grid} . d is the distance from the surface, d_0 is a variable determining the intensity of the near-surface grid zooming.

Thus, the function f is here chosen as the sum of four different components. The reason for this is to generate refined coordinate spacing in regions of strong stratification and strong shear, and near the surface. For avoiding too coarse coordinate spacing in regions with low shear and stratification far away from the surface, a background value is added. The choice for the four components (32)–(35) results from various numerical experiments, of which some are shown in Section 5. However, also other choices might be advantageous, such as the inverse of the turbulent macrolength scale or higher derivatives of shear and stratification. The gradients of T and S might be considered separately in order to obtain grid refinements also for the case of compensating T and S distributions. Even consideration of dynamically passive tracers such as geobiochemical quantities might be feasible, although the advantages might be questionable, since such constructions might be too complex and passive tracers often follow the density structure anyway.

4. Discretisation

As a first step of the spatial discretisation, the dynamic equations are integrated over vertical intervals. This may be done in the physical space (see Lander et al., 1994) or in the transformed

space (see Burchard and Petersen, 1997). The calculation of the adaptive grid will here be carried out in the normalised z -space (or σ -space), which is divided into I intervals. Let

$$-H = z_0 < z_1 < \dots < z_{I-1} < z_I = \zeta \quad (36)$$

be discrete interface levels such that the discrete layer thicknesses in the physical space can be calculated as:

$$h_i = (z_i - z_{i-1}), \quad 1 \leq i \leq I. \quad (37)$$

The grid is iteratively and implicitly updated at every time step by means of discretising the grid diffusion equation (30):

$$z_i^{n+1} = z_i^n + I^2 \Delta t^{\text{grid}} \left(k_{i+1}^{\text{grid}} (z_{i+1}^{n+1} - z_i^{n+1}) - k_i^{\text{grid}} (z_i^{n+1} - z_{i-1}^{n+1}) \right), \quad i = 1, \dots, I-1. \quad (38)$$

The baroclinic time step of the model is denoted by Δt . Here, Δt^{grid} is the grid diffusion time step which should be a fraction of the baroclinic model time step Δt :

$$j \Delta t^{\text{grid}} = \Delta t, \quad (39)$$

with j being an integer number. Thus, step (38) is repeated j times for every baroclinic time step Δt . As initial grid, an equidistant grid with

$$z_i^0 = D \left(\frac{i}{I} - 1 \right) \quad (40)$$

will be used for convenience. The discrete grid diffusivities K_ρ^{grid} and K_u^{grid} defined in (32) and (33) are linearly interpolated after every grid adaptation microtime step Δt^{grid} . In order not to obtain too thin discrete model layers, the grid related diffusivity k_i^{grid} was set to zero in the following case:

$$z_i - z_{i-1} < \frac{D}{1000I}. \quad (41)$$

For the vertical advection caused by the interfaces z_i moving at a discrete velocity

$$\left(J\tilde{\omega} \right)_i = w_i = - \frac{z_i^{n+1} - z_i^n}{\Delta t} \quad (42)$$

(see Eq. (24)), various monotone advection schemes will be tested. Among those is the first-order upwind scheme (which is known for its high numerical diffusion) and several total variation diminishing (TVD) schemes such as the second-order MUSCL scheme (van Leer, 1979), the second-order Superbee scheme (Roe, 1985) and the third-order P₂-PDM scheme (see Leonard, 1991). An overview over those schemes has been given by Pietrzak (1998).

The positivity of the turbulent quantities k and ε is guaranteed by the so-called source term linearisation suggested by Patankar (1980). The Coriolis rotation is carried out by means of an operator split method. The discretisation of the diffusion terms is done fully implicitly (including the grid diffusion equation) which requires the solution of tri-diagonal matrices by means of a simplified Gauss elimination.

5. Applications

The grid adaptation scheme described above (see Section 3), will be applied to five test scenarios, which are chosen in such a way that a wide range of one-dimensional oceanic processes is covered. These five scenarios are: an idealised wind entrainment experiment (see Section 5.1), an idealised free convection experiment (see Section 5.2), an idealised tidal flow experiment (see Section 5.3), a shelf sea experiment (Fladenground Experiment 1976 in the Northern North Sea, see Section 5.4) and an open ocean mixed layer experiment (Ocean Weather Station Papa in the Northern Pacific Ocean, see Section 5.5).

Among these test scenarios, the wind entrainment experiment is considered as a general test to investigate the impact of variations in the weighting of the effects of stratification and shear on the grid generation. Furthermore, this test case will be used for estimating the effects of different advection schemes for calculating the advection through the moving grid layers.

For all test scenarios, the evolution of shear frequency squared, M^2 , and Brunt–Väisälä frequency squared, N^2 , and the resulting grids for $I = 10, 20, 40$ and 80 layers will be displayed. Moreover, the errors of the results for current velocity and density of equidistant and adaptive grids for these resolutions in relation to a high-resolution equidistant grid will be displayed and discussed. The error between two discrete profiles a_i and b_i given on the same grid with layer thicknesses h_i is calculated as follows:

$$L_2(a, b) = \frac{\sqrt{\frac{1}{D} \sum_{i=1}^I (a_i - b_i)^2 h_i}}{\sqrt{\frac{1}{D} \sum_{i=1}^I (a_i - \bar{a})^2 h_i}}, \quad (43)$$

with the depth $D = \sum h_i$ and the mean

$$\bar{a} = \frac{1}{D} \sum_{i=1}^I a_i h_i. \quad (44)$$

Here, a_i is the high-resolution reference solution. The normalised error L_2 measures the standard deviation of the error compared to the standard deviation of the solution. For discrete profiles given on different grids, the two profiles are first transformed to a fine grid which includes both other grids as under sets and then treated with method (43).

For all test scenarios, the reference density difference is set to $\Delta\rho = 0.2 \text{ kg m}^{-3}$, the reference velocity difference to $\Delta u = 0.2 \text{ m s}^{-1}$. The other parameters determining the grid adaptation are given in Table 1. As vertical advection scheme, the P_2 -PDM scheme has been used unless stated differently.

Table 1

Grid adaptation parameters for five methods used for the wind entrainment experiment, see Section 5.1

	c_ρ	c_u	c_d	c_b	T^{grid} (s)	c
Method 1	0.8	0.0	0.1	0.1	3600	0.01
Method 2	0.6	0.2	0.1	0.1	3600	0.01
Method 3	0.4	0.4	0.1	0.1	3600	0.01
Method 4	0.2	0.6	0.1	0.1	3600	0.01
Method 5	0.0	0.8	0.1	0.1	3600	0.01

5.1. Wind entrainment experiment

In this basic experiment, first carried out in a laboratory by Kato and Phillips (1969), a mixed layer induced by a constant surface stress penetrates into a stably stratified fluid with density increasing linearly down from the surface. The water depth is assumed to be infinite. Price (1979) suggested a solution for the evolution of the mixed-layer depth D_m based on a constant Richardson number

$$D_m(t) = 1.05u_*^s N_0^{-1/2} t^{1/2}, \quad (45)$$

where u_*^s is the surface friction velocity and N_0 , the constant initial Brunt–Väisälä frequency. Following several authors (see e.g. Deleersnijder and Luyten, 1994; Burchard et al., 1998) we

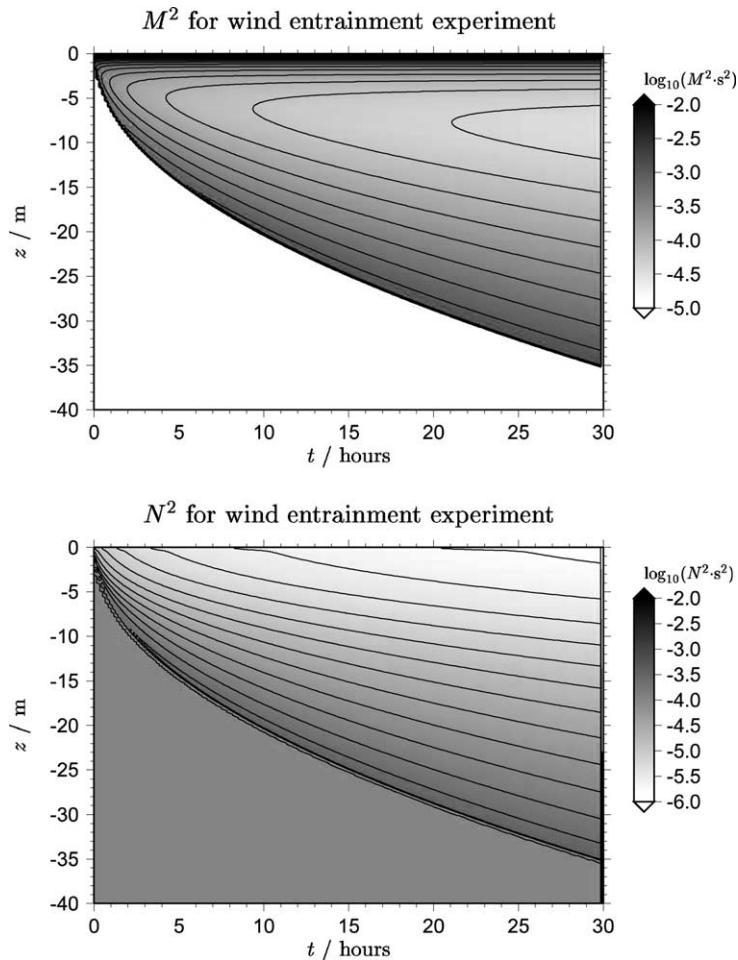


Fig. 1. Wind entrainment experiment: shear-frequency squared (M^2) and Brunt–Väisälä frequency squared (N^2) in logarithmic scale computed by a high-resolution Cartesian grid with $\Delta z = 0.125$ m and $\Delta t = 1$ s.

transform this laboratory experiment to oceanic dimensions with $u_*^s = 10^{-2} \text{ m s}^{-1}$ and $N_0 = 10^{-2} \text{ s}^{-1}$.

For this entrainment experiment, five different parameter combinations for the grid generation method from Eq. (30) have been tested, see Table 1.

Method 1 does not consider shear for the grid generation whilst method 5 does not consider stratification. The methods 2, 3 and 4 interpolate between these extremes by means of weighting parameters. The influence of the distance from the surface and the background value are kept the same for all methods, as well as the time scale T^{grid} . These choices are results of various numerical experiments. A higher background value would increase the tendency towards equidistant grids, longer adaptation time scales T^{grid} would result in a slower reaction of the grid lines to changes in the internal fields. In contrast to that, too short time scales have the consequence of destabilising the numerical solution.

The evolution of shear frequency squared, M^2 , and Brunt–Väisälä frequency squared, N^2 , for this wind entrainment experiment are shown in Fig. 1. Clearly, M^2 has a maximum near the surface due to the surface stress forcing and a further maximum in the entrainment layer due to vanishing friction. Below the entrainment layer, there is no shear. The stratification (N^2) increases

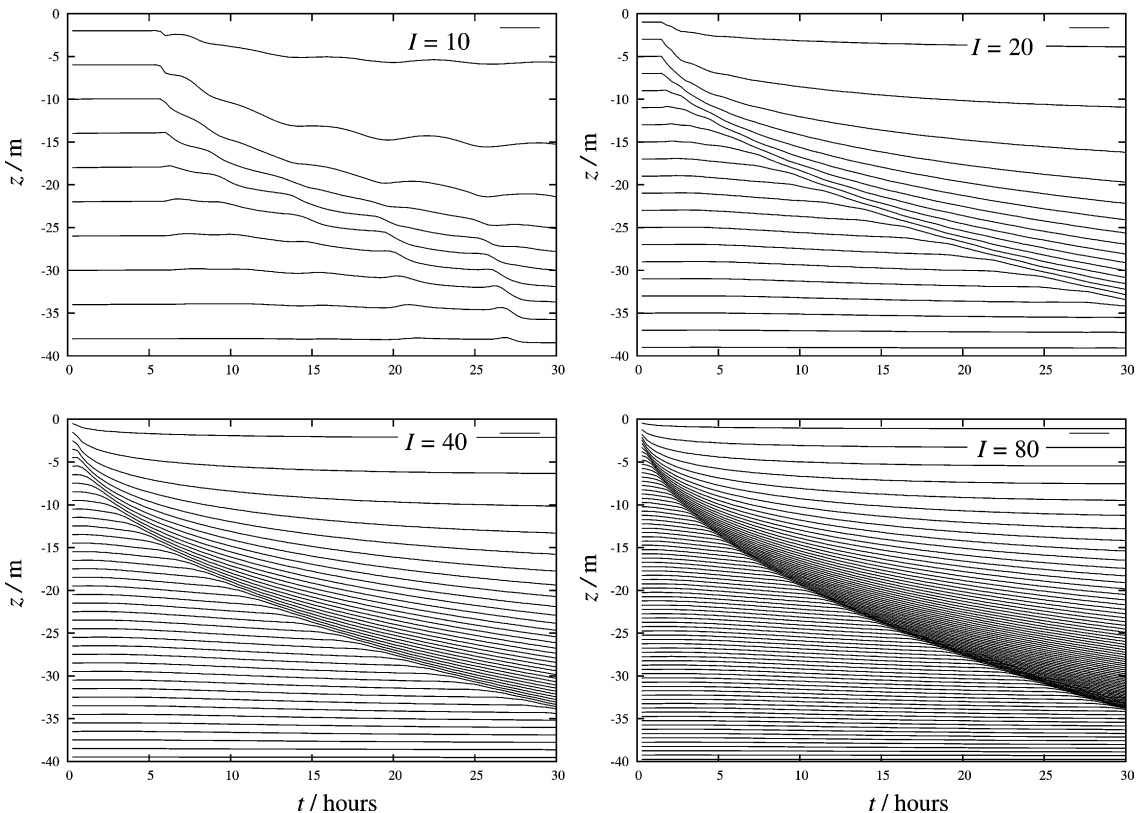


Fig. 2. Wind entrainment experiment: adaptive grids for various number of layers which have been computed by means of method 1.

continuously down from the surface until a local maximum in the entrainment layer below which the prescribed initial value of $N^2 = 10^{-4} \text{ s}^{-2}$ is reached.

The grid adaptation time step used here is $\Delta t = 5 \text{ s}$, and the time steps are $\Delta t = 300 \text{ s}$ for $I = 10$, $\Delta t = 80 \text{ s}$ for $I = 20$, $\Delta t = 20 \text{ s}$ for $I = 40$, and $\Delta t = 5 \text{ s}$ for $I = 80$.

The effect of the different grid adaptation parameters and the associated errors for this wind entrainment experiment are shown in Figs. 2–7. Due to the local maxima of shear and stratification, all five grid generation schemes calculate refined grids in the area of the entrainment layer. As expected, the density error is small for a strong impact of stratification on the grid adaptation and the velocity error is small for a strong impact of shear. Only for the method 5 with no buoyancy effect, both the density error and the velocity error are larger than the error for the respective equidistant grids (see Fig. 7). For method 2, both the density and the velocity error of the adaptive grids are smaller than the respective equidistant grids with the same number of layers, for method 3, the velocity error of the adaptive grid is much smaller than for the equidistant grid, but this is just not the case for the density error. Since method 3 provides a balanced weighting between shear and stratification effects on the grid generation, we will apply this method to all four following test cases (see Sections 5.2–5.5).

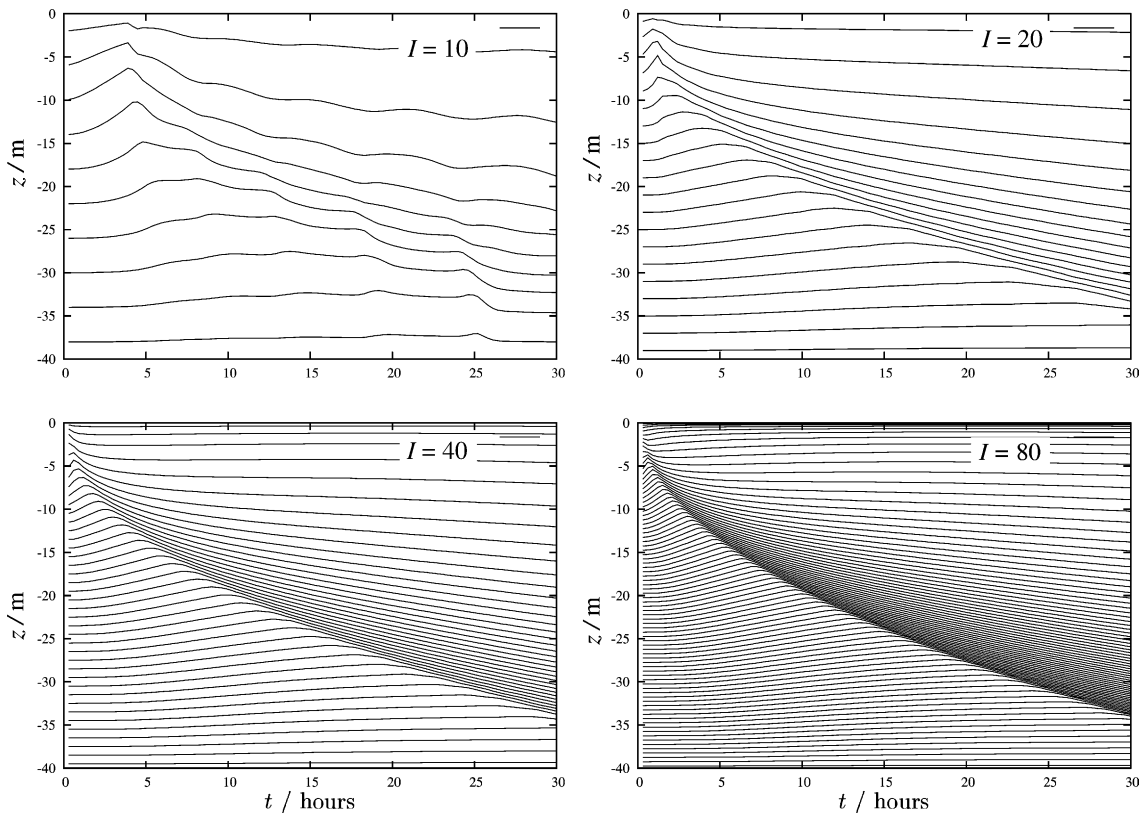


Fig. 3. Wind entrainment experiment: adaptive grids for various number of layers which have been computed by means of method 2.

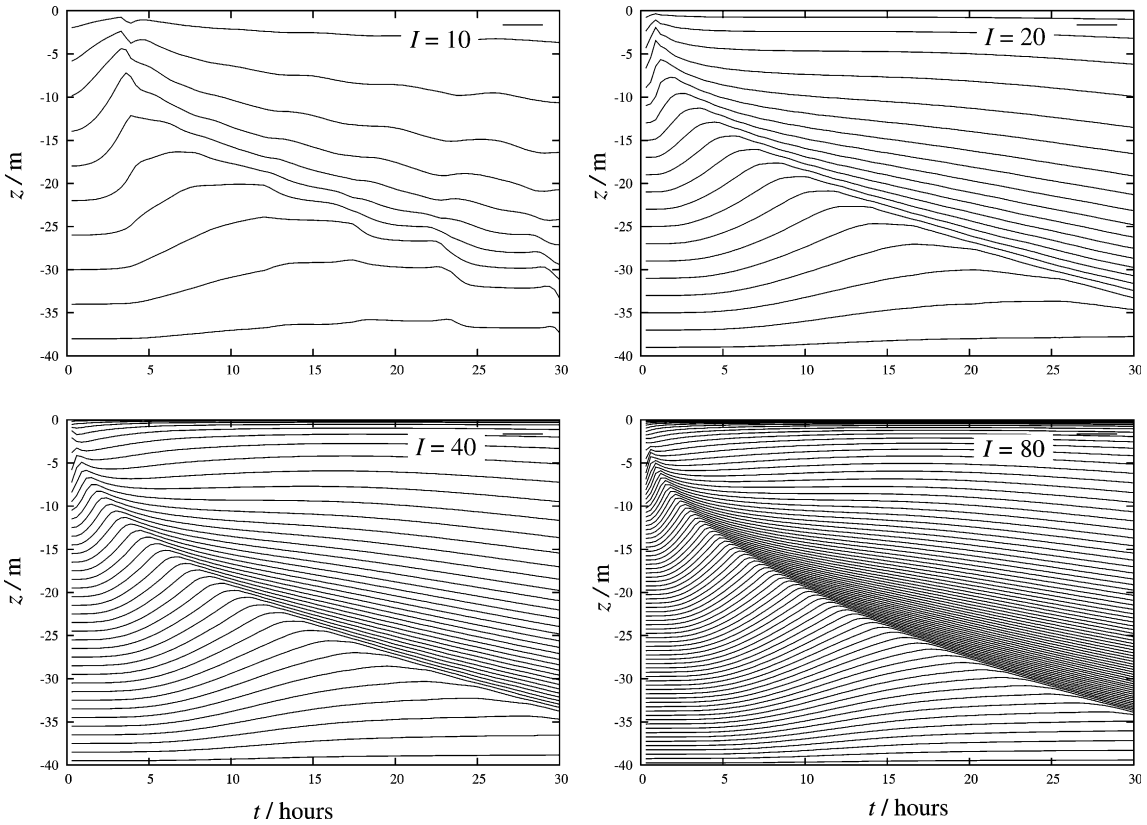


Fig. 4. Wind entrainment experiment: adaptive grids for various number of layers which have been computed by means of method 3.

It should be noted that the positive effect of an optimal distribution of grid layers in time and space will be partially compensated by numerical advection errors inevitably connected to advection schemes. For the one-dimensional cases considered here, such advection error do not occur for Cartesian coordinates since there is no physical advection. In order to assess the impact of the advection error, a passive concentration profile

$$d(z) = C(-z)^{1/2} \left(1 + \frac{z}{D} \right) \quad (46)$$

with $C = 0.00164$ which remains constant in time due to lack of vertical mixing is calculated by means of the adaptive grids generated with method 3, see Fig. 4. Fig. 8 shows the resulting profiles for the P_2 -PDM scheme for various vertical resolutions. Initial discrete values are obtained by calculating analytically the layer means of d . This generates an initial interpolation error which is identical for equidistant and adaptive grids. Especially for the low resolution case ($I = 10$), significant deviations from the exact solution are visible. A quantification of this advection error is shown in Fig. 9 for four different advection schemes in comparison to the pure interpolation error

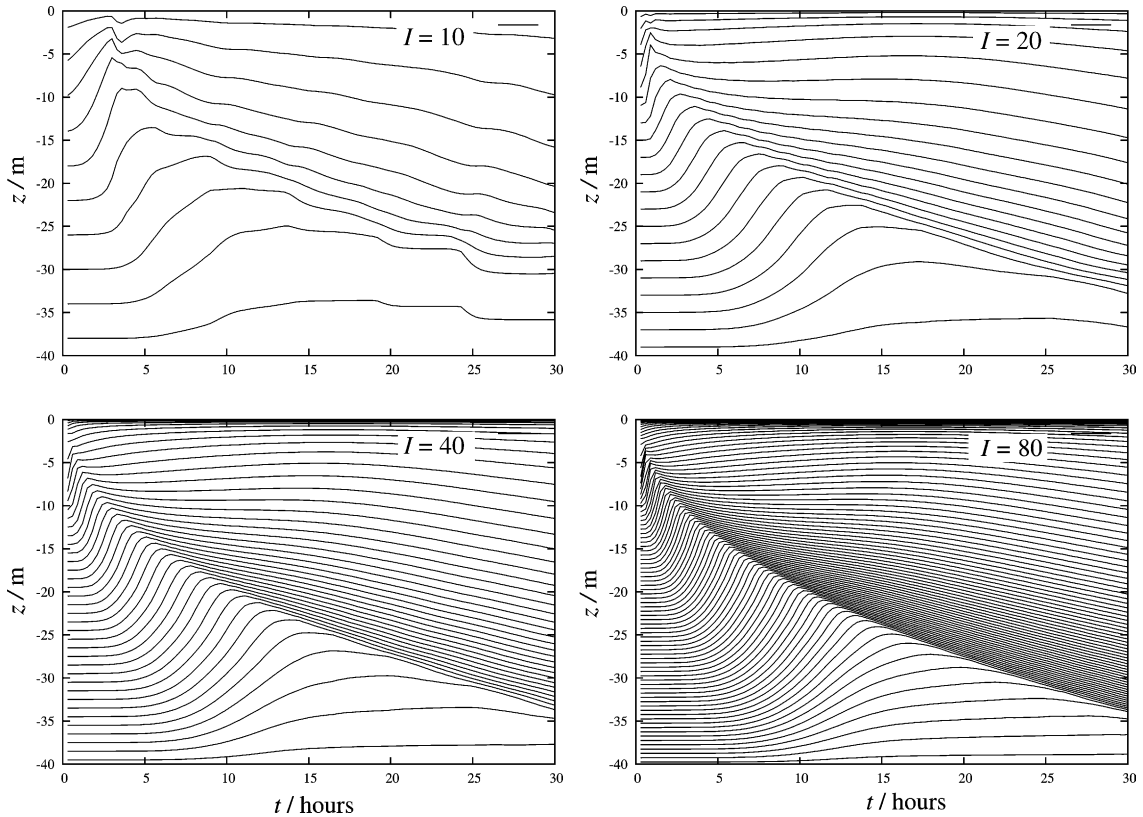


Fig. 5. Wind entrainment experiment: adaptive grids for various number of layers which have been computed by means of method 4.

caused by the equidistant Cartesian grid. The error obtained by the first-order upstream scheme is clearly the largest. In contrast to that, the error for the TVD schemes are much smaller. Among those, the Superbee scheme which is known to overestimate gradients is the worst. The other two TVD schemes (the MUSCL scheme and the P_2 -PDM) perform almost identically and not much worse than the equidistant Cartesian grid. As a consequence of this, the P_2 -PDM scheme will be used for the following test cases.

5.2. Free convection experiment

In order to test the performance of the proposed grid generation algorithm for shear-free, convective turbulence, a simulation motivated by the laboratory experiment by Willis and Deardorff (1974), is carried out here. This scenario is the same as used by Large et al. (1994). By means of a constant negative surface heat flux of 100 W m^{-2} , a convective boundary layer is entrained into a stably stratified ocean with a surface temperature of $22 \text{ }^\circ\text{C}$ and a temperature

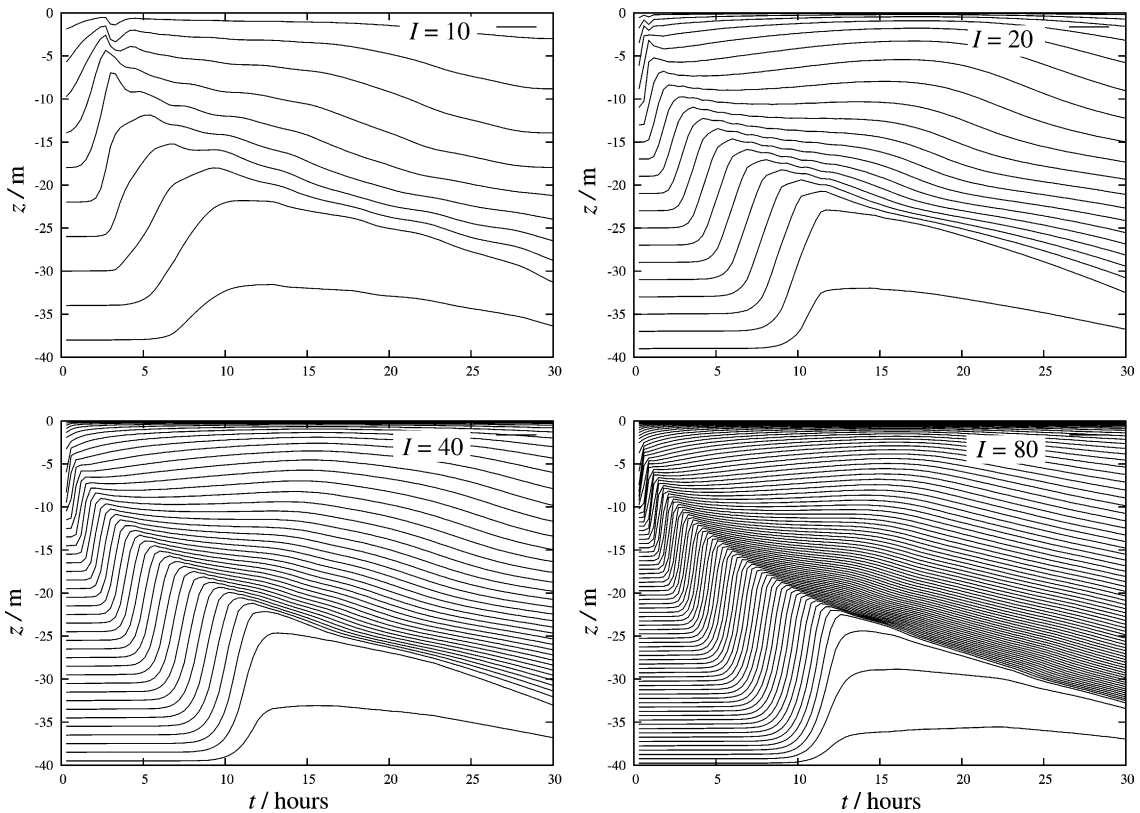


Fig. 6. Wind entrainment experiment: adaptive grids for various number of layers which have been computed by means of method 5.

gradient of $1\text{ }^{\circ}\text{C}$ per 10 m . Shear and rotation are not present. For this free convection simulation recent large Eddy simulation (LES) data are available from Mironov et al. (2001). Numerical simulations with two-equation turbulence closure models have been performed by Burchard and Bolding (2001).

The stratification N^2 for this free-convection scenario is shown in Fig. 10. In the convectively mixed layer, the stratification is unstable, in the entrainment layer, a local maximum of N^2 is reached and below, the initially prescribed constant stratification remains.

As grid adaptation method, almost the same settings as for the wind entrainment experiment with method 3 have been used. The differences are a larger $T^{\text{grid}} = 10,600\text{ s}$ and $d_0 = 15\text{ m}$. The grid adaptation time step used here is $\Delta t = 2\text{ s}$, and the time steps are $\Delta t = 512\text{ s}$ for $I = 10$, $\Delta t = 128\text{ s}$ for $I = 20$, $\Delta t = 32\text{ s}$ for $I = 40$, and $\Delta t = 8\text{ s}$ for $I = 80$. Fig. 11 clearly shows how the grid lines are focused around the entrainment layer where higher resolution is needed. Furthermore, a small enhancement of resolution is also obtained in the near-surface region where the K_d^{grid} has a maximum. Compared to equidistant grids, the error is significantly smaller for adaptive grids (see Fig. 12). The reason for the better performance of the adaptive grids compared to the wind entrainment case from Section 5.1 is probably that here the vertical displacement velocity is

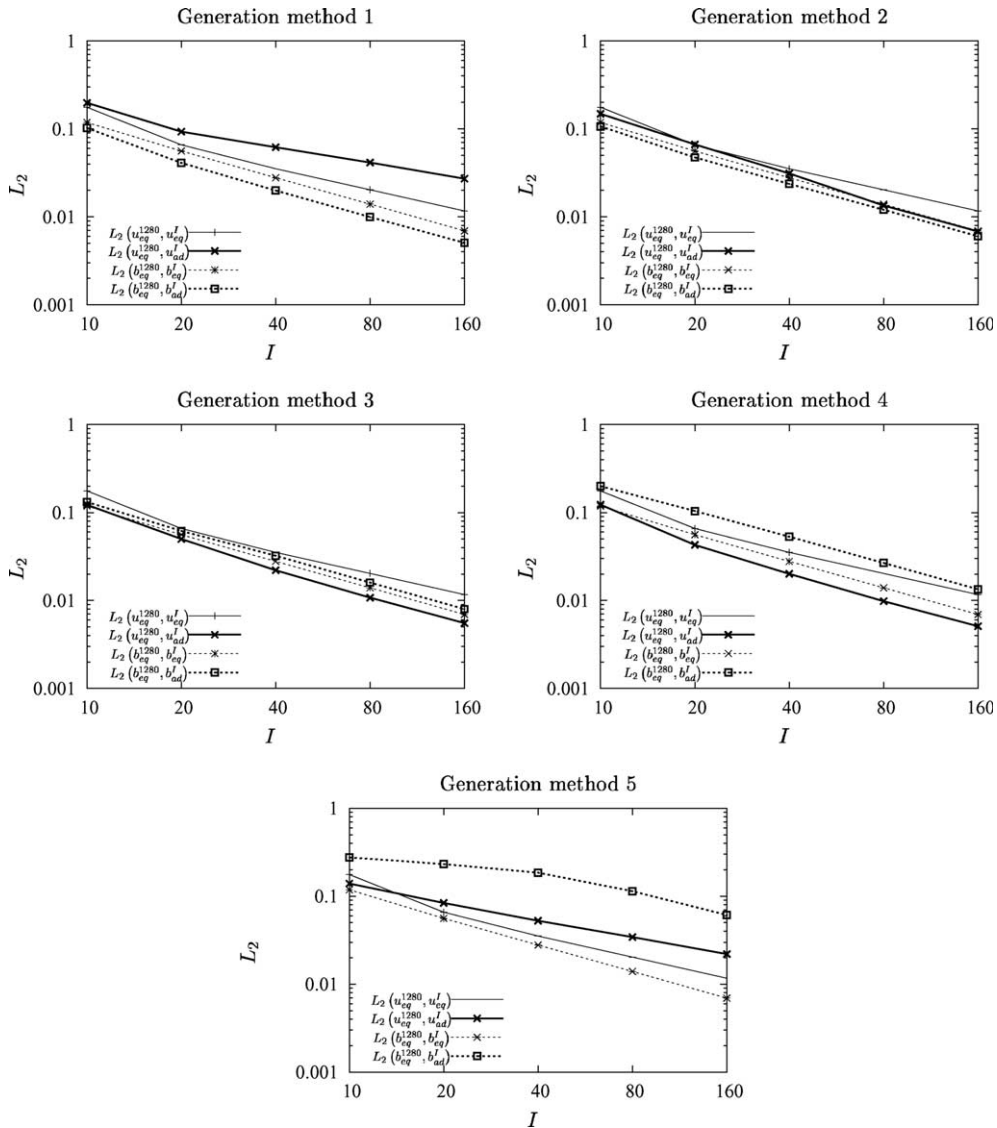


Fig. 7. Wind entrainment experiment: integral rms errors between results for several resolutions for the adaptive grid methods 1–5 and the equidistant grid, both in relation to the high resolution ($I = 1280$) equidistant solution.

smaller due to gentle surface forcing in contrast to the sudden onset of a surface stress in the latter case.

In Fig. 13, the reproduction of the mixed layer depth (diagnosed from the lowest location with a turbulent kinetic energy of $k > 1 \times 10^{-8} \text{ J kg}^{-1}$) is shown for the equidistant and the adaptive grids. It can be clearly seen that the ability of the adaptive grid to partially track structures leads to a significantly more exact reproduction of the mixed layer depth.

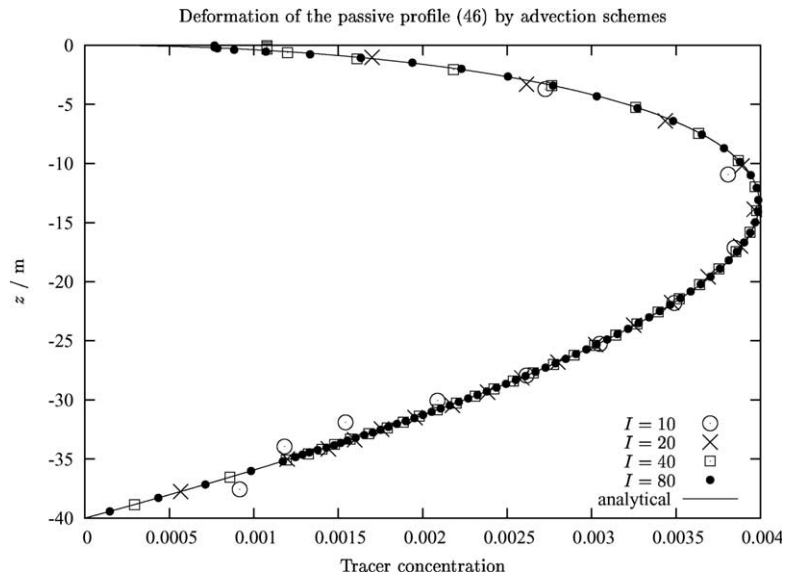


Fig. 8. Resulting final (after $t = 30$ h) profiles of a passive and physically not advected nor diffused tracer from the numerical grids in Fig. 4 in relation to the initial, analytical solution.

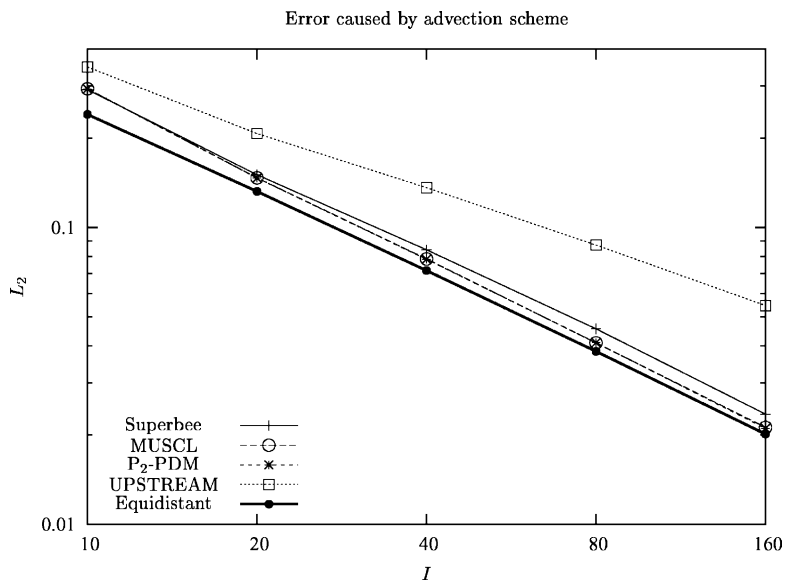


Fig. 9. Integral rms errors between results for several resolutions and several advection methods in relation to the analytical solution for the passive tracer, see Fig. 4. This shows the error due to coordinate line advection. The equidistant grid curve shows the pure interpolation error which is minimised by this integral error measure.

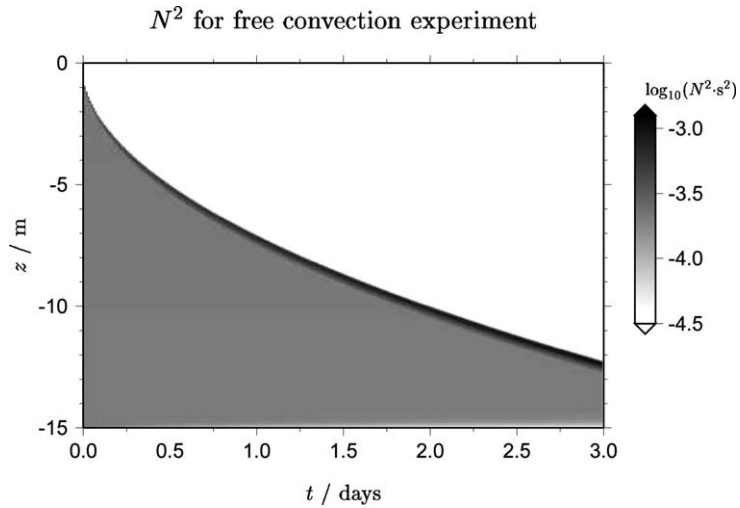


Fig. 10. Free convection experiment: Brunt–Väisälä frequency squared (N^2) in logarithmic scale computed by a high-resolution Cartesian grid with $\Delta z = 0.046875$ m and $\Delta t = 1$ s. Areas with unstable stratification are displayed in white.

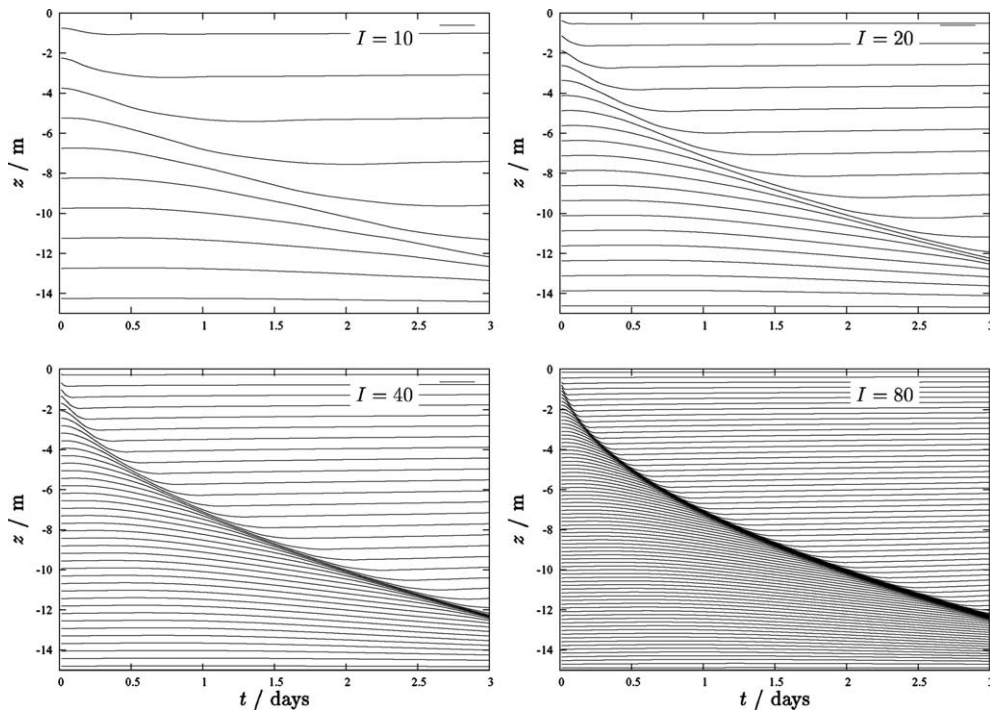


Fig. 11. Free convection experiment: adaptive grids for 10, 20, 40 and 80 layers which have been computed by means of method 3.

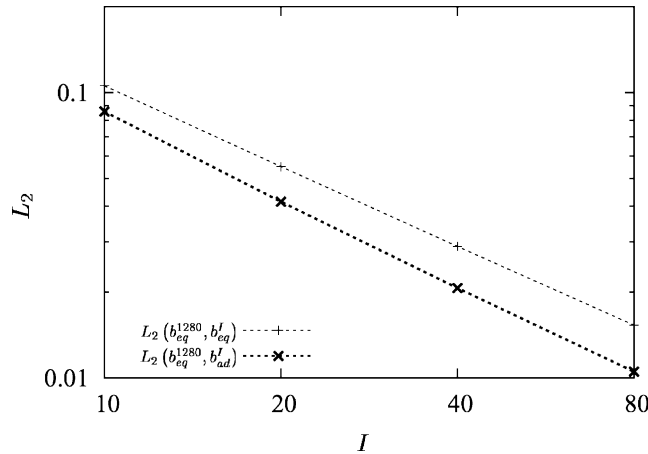


Fig. 12. Free convection experiment: integral rms errors between results for four resolutions for the adaptive grid (method 3) and the equidistant grid, both in relation to the high resolution ($I = 1280$) equidistant solution.

5.3. Idealised tidal flow

This idealised tidal flow experiment simulates a simple open channel flow forced by a periodically oscillating surface slope. The water depth is $D = 15$ m, the tidal period is the semi-diurnal lunar tide ($T = 44,714$ s) and the amplitude of the surface slope is $(\partial_x^* \zeta)_{\max} = 5 \times 10^{-4}$ with an offset of -2×10^{-4} resulting in a residual flow into the negative x -direction. Rotation and stratification are not considered.

Fig. 14 shows the shear squared, M^2 , for this experiment during the fourth tidal period after initialising the model from rest. As expected, M^2 varies over a range of several orders of magnitude, with short phases of nearly shear-free flow around the slack tides.

As grid adaptation method, almost the same settings as for the wind entrainment experiment with method 3 have been used. The only difference is a smaller $d_0 = 15$ m. The grid adaptation time step used here is $\Delta t = T/64,000$, and the time steps are $\Delta t = T/1000$ for $I = 10$, $\Delta t = T/4000$ for $I = 20$, $\Delta t = 16,000$ for $I = 40$, and $\Delta t = T/64,000$ for $I = 80$. After the three tidal periods of model spin-up, a clear zooming of layers towards the bottom is visible for all experiments shown in Fig. 15. In contrast to that, the temporal variability of the grid layer is relatively small, because the shape of the velocity profile will be most of the time close to a logarithmic profile which varies in intensity. Thus the major change in time is the relative weighting of the background diffusion and the shear-related diffusion. The error of the adaptive grids is significantly smaller than those of the respective equidistant grids, see Fig. 16. However, when the equidistant grids are fine enough to resolve the near-bed layer properly (as for $I = 80$ layers), then the advantage of the adaptive grids is small.

5.4. Shelf sea dynamics

As a shelf sea test case, a scenario from the Northern North Sea has been chosen here. This dataset which has been used throughout the last 20 years as a calibration for mixing

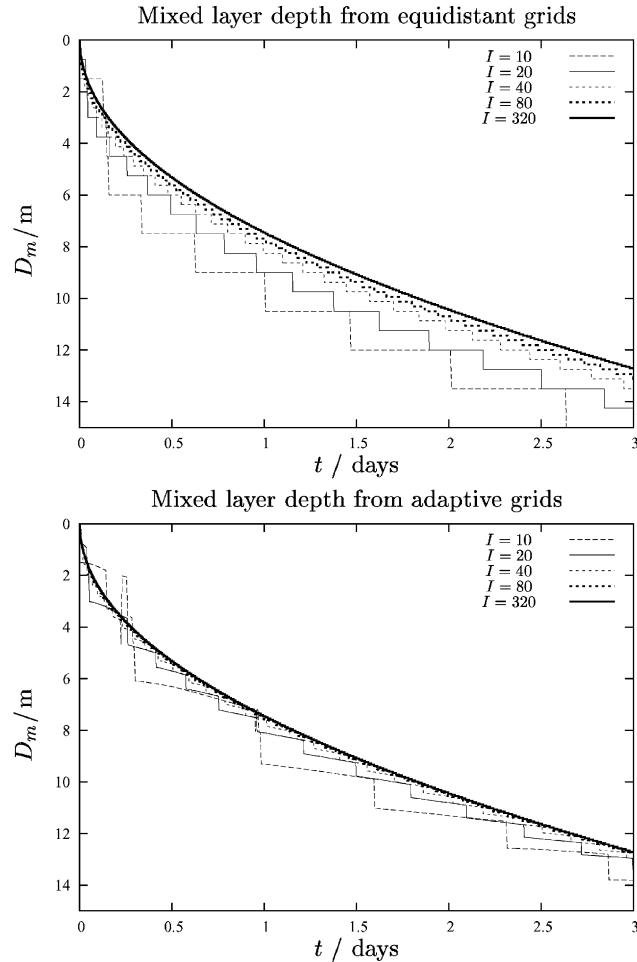


Fig. 13. Free convection experiment: mixed layer depth D_m of the convective boundary layer diagnosed from the lowest location with a TKE of $k > 1 \times 10^{-8} \text{ J kg}^{-1}$ calculated with equidistant and adaptive grids. Both solutions are compared to a high-resolution equidistant solution with $I = 320$ layers.

parameterisations has been collected during the measurements of the Fladengrund Experiment 1976 (FLEX'76) campaign. The measurements of meteorological forcing and temperature profiles were carried out in spring 1976 in the northern North Sea at a water depth of about 145 m and a geographical position at $58^{\circ}55' \text{ N}$ and $0^{\circ}32' \text{ E}$. For further details concerning the measurements, see Soetje and Huber (1980) and Brockmann et al. (1984). This FLEX'76 dataset has been used by several authors in order to test different mixing schemes (see e.g. Friedrich, 1983; Frey, 1991; Burchard and Baumert, 1995; Pohlmann, 1997; Burchard and Petersen, 1999; Mellor, 2001).

The high-resolution solutions for M^2 and N^2 are shown in Fig. 17. From an initially weakly stratified water column around day 100, a two-layer structure is developing due to the general heating of the near-surface waters and the interaction of stratification with vertical mixing. It can

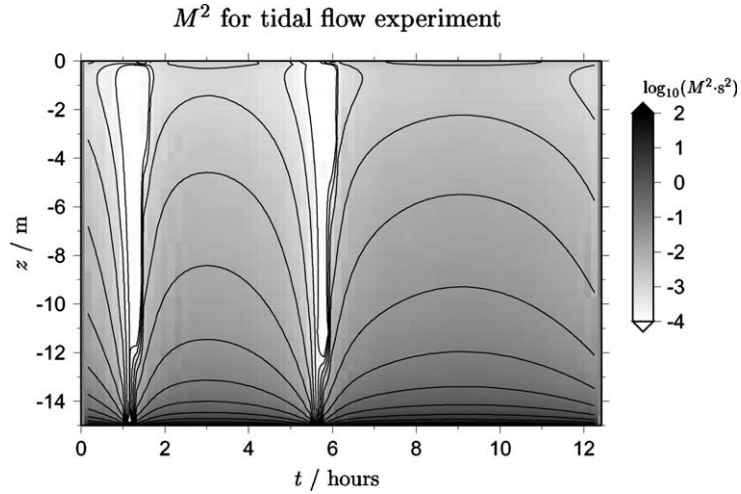


Fig. 14. Tidal flow experiment: shear-frequency squared (M^2) in logarithmic scale computed by a high-resolution Cartesian grid with $\Delta z = 0.046875$ m and $\Delta t = 1$ s. For $1 < t < 5$ h, the flow is against the residual flow, and for $t > 6$ h, the flow is with the residual flow.

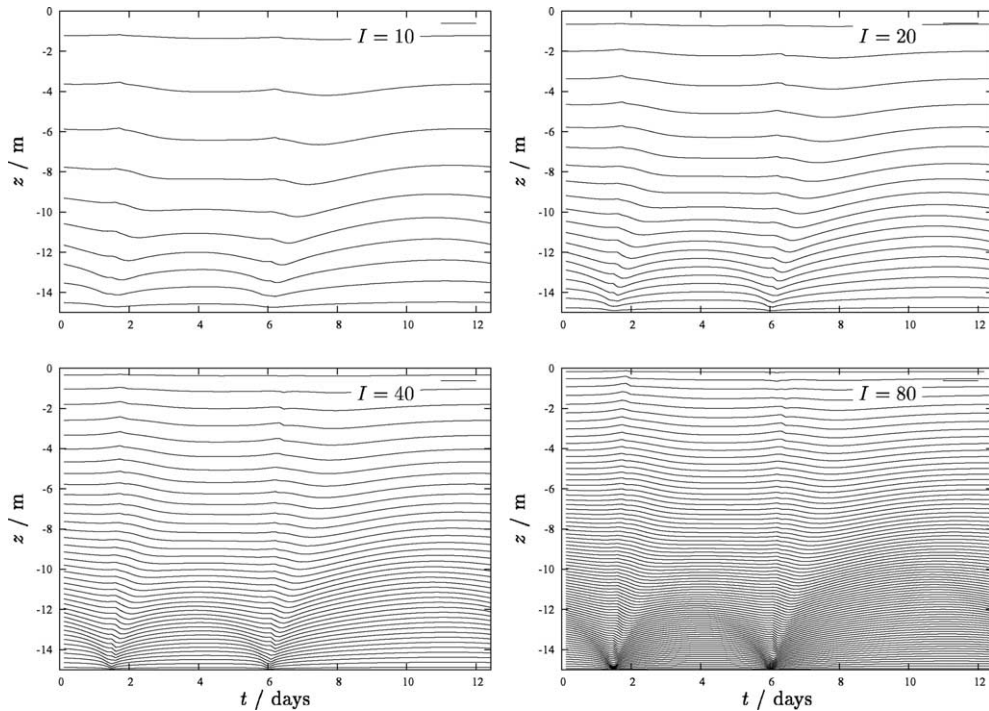


Fig. 15. Tidal flow experiment: adaptive grids for 10, 20, 40 and 80 layers which have been computed by means of method 3.

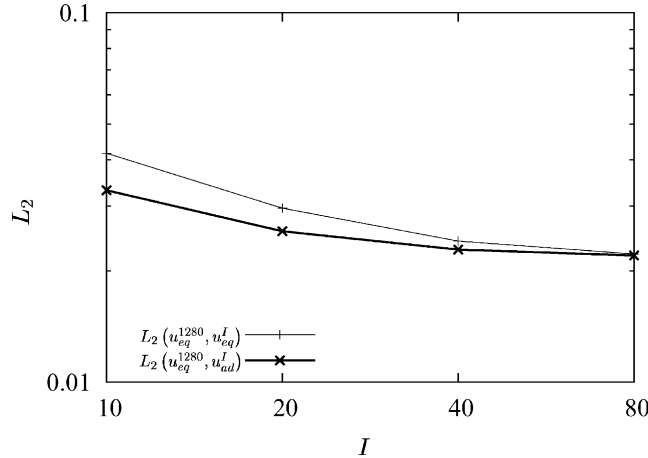


Fig. 16. Tidal flow experiment: integral rms errors between results for three resolutions for the adaptive grid (method 3) and the equidistant grid, both in relation to the high resolution ($I = 1280$) equidistant solution.

be seen that generally the shear increases where the stratification is high, which occurs due to decreased vertical mixing. Additionally, shear is high near the surface due to wind stress and near the bottom due to tidally generated bottom stress. A typical feature of this shelf sea scenario is the strong wind event on day 133, which mixes the upper 50 m of the water column.

Some instabilities may be identified at the bottom of the mixed layer. These are physically caused by the complex second moment closure which depends on shear and stratification (see Canuto et al., 2001). It can be shown that these instabilities do not vanish for small time steps, see also the discussion by Burchard and Deleersnijder (2001) who argue that these instabilities may be removed by using simpler quasi-equilibrium versions of the second moment closure models.

As grid adaptation method, again almost the same settings as for the wind entrainment experiment with method 3 have been used. The only difference is a larger time scale $T^{\text{grid}} = 2$ days and a smaller $d_0 = 10$ m. The grid adaptation time step used here is $\Delta t = 5$ s, and the time steps are $\Delta t = 300$ s for $I = 10$, $\Delta t = 80$ s for $I = 20$, $\Delta t = 20$ s for $I = 40$, and $\Delta t = 5$ s for $I = 80$.

The resulting adaptive grids are shown in Fig. 18. It can be clearly seen how the grid lines follow regions of strong shear and stratification. The tidal oscillations appear as short oscillations of the grid lines in the lower half of the water column, see the grid for $I = 80$ layers. The way that the grid lines follow the internal structure of the flow, may be studied in detail by means of Fig. 19, where the area of the strong wind event is highlighted and shear and stratification are overlaid with grid lines for the numerical experiment with $I = 20$ layers. Changes in the internal flow structure are immediately sensed by the adaptive grid generation scheme, but the structures are not exactly traced. This is due to the grid adaptation time scale which prevents vertical grid motion from being too fast and producing increased vertical advection errors and possible numerical instabilities. A too direct adaptation would lead to increased vertical advection errors and numerical instabilities.

The overall error of the numerical simulations compared to a high-resolution solution is significantly improved by the adaptive grids for both, the velocity and the density fields, see Fig. 20.

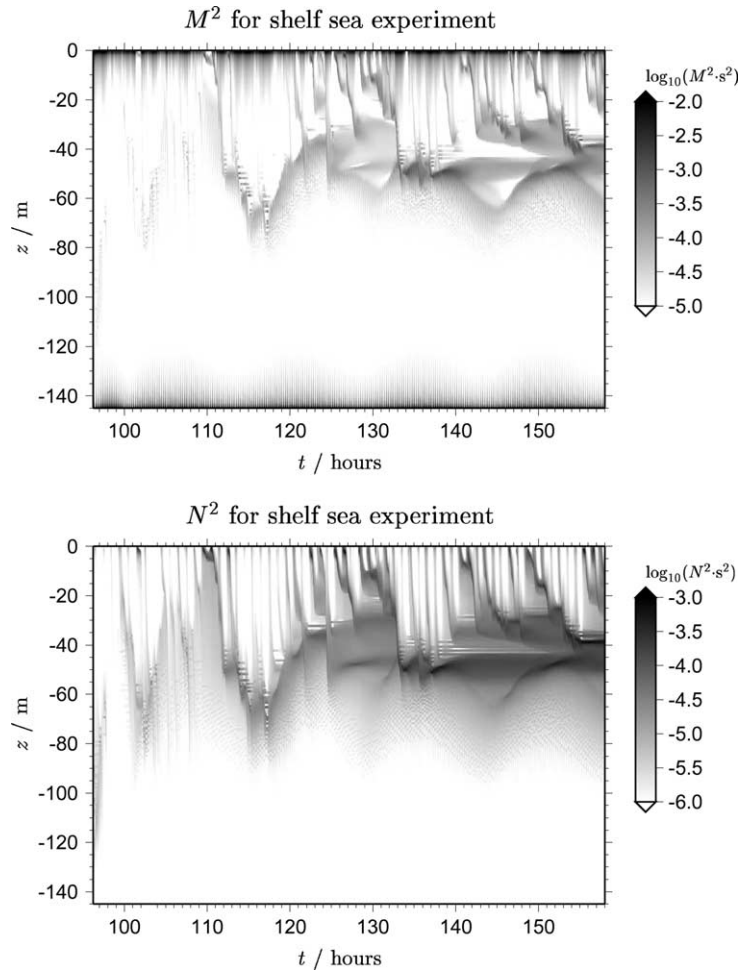


Fig. 17. Shelf sea experiment: shear-frequency squared (M^2) and Brunt-Väisälä frequency squared (N^2) in logarithmic scale computed by a high-resolution Cartesian grid with $\Delta z = 0.5$ m and $\Delta t = 1$ s.

5.5. Open ocean mixed layer

For the open ocean, long term observations of meteorological parameters and temperature profiles are available from several stations. The OWS Papa, located in the Northern Pacific Ocean at 145° W, 50° N has the advantage that it is situated in a region where the horizontal advection of heat and salt is assumed to be small. Various authors used these data for validating turbulence closure schemes (Denman, 1973; Martin, 1985; Gaspar et al., 1990; Large et al., 1994; Kantha and Clayson, 1994; D'Alessio et al., 1998; Burchard et al., 1999; Villarreal, 2000; Axell and Liungman, 2001; Burchard and Bolding, 2001). The basic setup for this simulation which generally follows the simulations carried out by Large et al. (1994) is described in detail in by Burchard et al. (1999). The upper 250 m of the water column for which temperature profile observations are available are reproduced between March 1961 and March 1962.

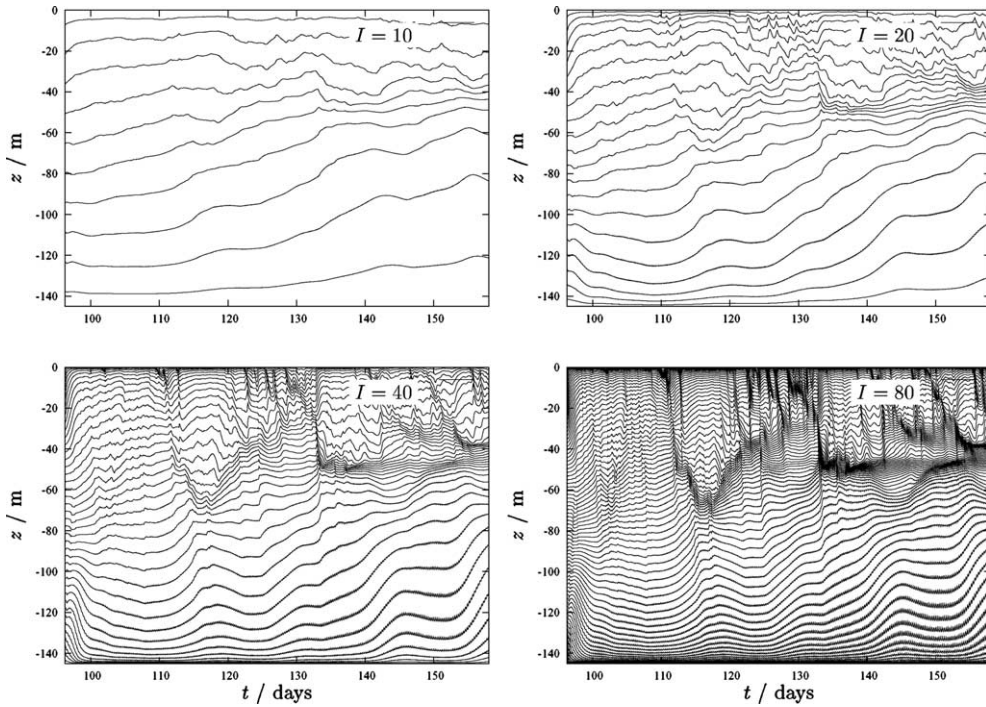


Fig. 18. Shelf sea experiment: adaptive grids for 10, 20, 40 and 80 layers which have been computed by means of method 3.

Fig. 21 shows M^2 and N^2 for this final test scenario. The shallowing of the mixed layer during the summer season is clearly seen in both quantities. The instabilities due to the second-moment closure which have already been discussed for the shelf sea scenario (see Section 5.4) are evident here as well.

As grid adaptation method, almost the same settings as for the wind entrainment experiment with method 3 have been used. The only difference is a larger time scale $T^{\text{grid}} = 7$ days and a smaller $d_0 = 10$ m. The grid adaptation time step used here is $\Delta t = 5$ s, and the time steps are $\Delta t = 1600$ s for $I = 10$, $\Delta t = 400$ s for $I = 20$, $\Delta t = 100$ s for $I = 40$, and $\Delta t = 25$ s for $I = 80$.

The resulting adaptive grids do again follow the major internal structures of the flow, see Fig. 22. Even the peculiarity visible at a water depth of about 100 m between days 100 and 150 is followed by the fine-resolution adaptive grid with $I = 80$ layers. In contrast to that, the inactive deeper parts of the water column with depths below 200 m are resolved with a coarse grid spacing only. Apart from the adaptive grid with $I = 80$ layers, the errors of the adaptive grids are smaller than those for the respective equidistant grids, see Fig. 23. The relatively small advantage of the adaptive grids for the reproduction of the density structure might be due to the coarse resolution in the deeper layers. This could be improved by choosing a different weighting between the impact of shear and stratification on the grid generation methods.

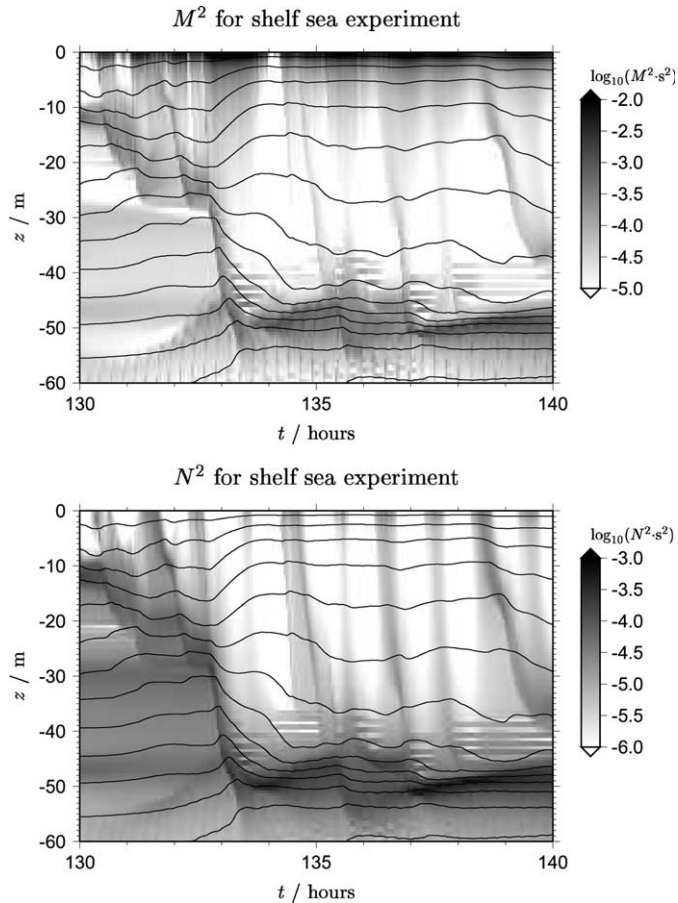


Fig. 19. Shelf sea experiment, detail showing a storm and its impact on shear and stratification: shear-frequency squared (M^2) and Brunt–Väisälä frequency squared (N^2) in logarithmic scale computed by a high-resolution Cartesian grid with $\Delta z = 0.5$ m and $\Delta t = 1$ s. The plots are overlaid with the grid lines for the case of $I = 20$ layers.

6. Conclusions and perspectives

It has been demonstrated here that the concept of general vertical coordinates can be exploited in such a way that adaptive grids can be used even in a one-dimensional framework. These grids which are based on a variational approach are generated by means of a coordinate diffusion equation which modifies the vertical position of grid interfaces in every time step according to the actual vertical flow structure. For all five test cases considered in this paper, these adaptive grids lead to a better global approximation of high-resolution solutions in comparison to the respective equidistant grids. Interestingly, it is not only the global error which is reduced by means of the grid adaptation, but also special features such as the mixed layer depth are better tracked, as shown for the free convection experiment. The grid adaptation method has been constructed in such a way that stable numerical solutions are obtained. This is done by means of introducing an

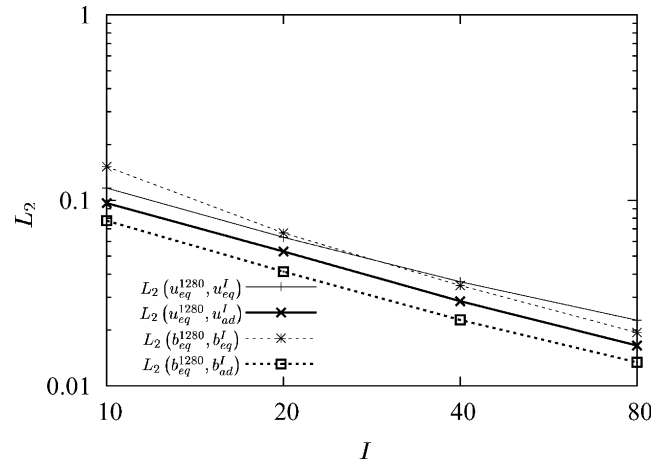


Fig. 20. Shelf sea experiment: integral rms errors between results for three resolutions for the adaptive grid (method 3) and the equidistant grid, both in relation to the high resolution ($I = 1280$) equidistant solution.

adaptation time scale which avoids too direct response of the grid generation to changes of the internal flow structure.

In this one-dimensional framework where the physical vertical velocity is zero, the introduction of a grid-related vertical advection does first of all lead to an additional truncation error due to the advection schemes. It could be shown how this error can be minimised by applying high-order advection schemes such as TVD schemes. This additional truncation error is however positively over-compensated by the better spatial arrangement of the grid lines. For one-dimensional models, the additional treatment of vertical advection with high-order schemes and the calculation of an additional diffusion equation for the grid adaptation means a significant computational overhead compared to model simulations with non-moving grids. However, when neglecting the additional computational costs for the vertical advection routines (which have to be used in three-dimensional models anyway), the overhead for the grid adaptation reduces to moderate 26% for the wind entrainment experiment. Most of this overhead is spent for the interpolation of M^2 and N^2 onto the new grid, a routine which was computationally not optimised in our implementation.

In three-dimensional models however, vertical advection is generally present and needs to be calculated anyway. Thus, there is no computational overhead with respect to grid-related vertical advection. Moreover, the truncation error for the vertical advective terms (which depends on the intensity of the grid related vertical velocity and the vertical gradients of the advected quantity) will be generally reduced by means of adaptive grids since they will tend to follow vertically moving physical interfaces such as isopycnals in a pseudo-Lagrangian way.

For three-dimensional models, these grid adaptation methods also open the way for almost-isopycnal coordinates including turbulent mixing, in contrast to classical isopycnic models which need some additional parameterisations to deal with vertical mixing.

Although the highest benefit of vertically adaptive grids will be obtained for three-dimensional models, also for one-dimensional models improvements could be demonstrated. One-dimensional models do thus provide a computationally cheap framework for testing new grid adaptation techniques.

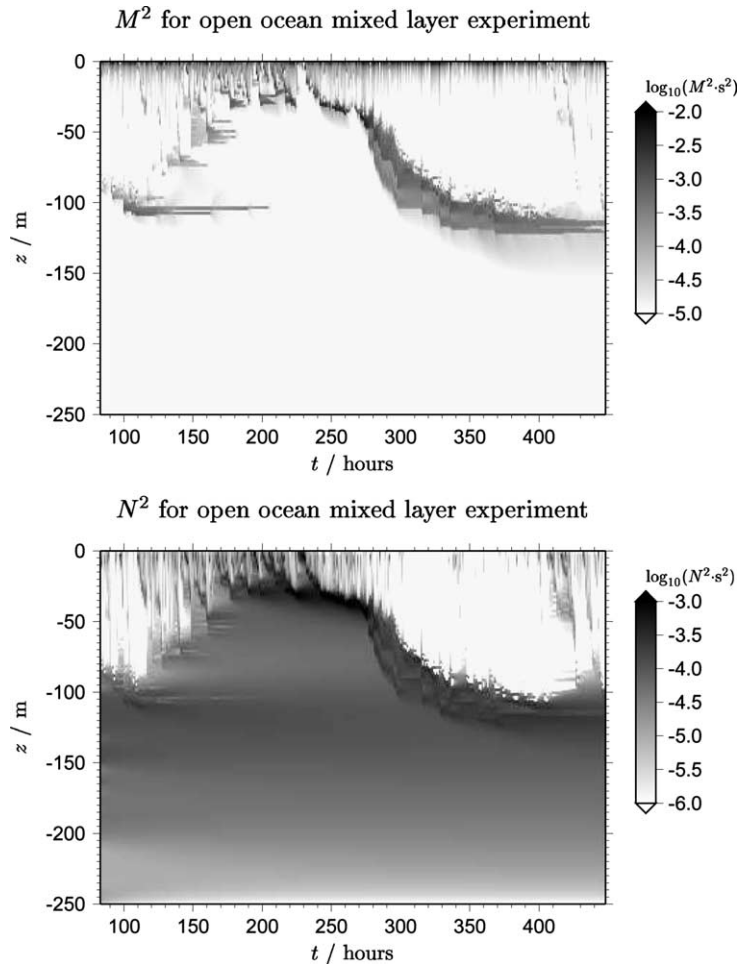


Fig. 21. Open ocean mixed layer experiment: shear-frequency squared (M^2) and Brunt–Väisälä frequency squared (N^2) in logarithmic scale computed by a high-resolution Cartesian grid with $\Delta z = 1$ m and $\Delta t = 5$ s.

Once a three-dimensional model is written in general vertical coordinates, this concept of adaptive grids can be easily implemented, since only the grid generation routines have to be modified. In addition to vertical gradients, also horizontal gradients of the physical fields and the numerical grid need to be considered for the grid adaptation in three-dimensional models. Since the grid adaptation is purely vertical, a front which has both a strong horizontal and vertical component (as in the case of an outcropping isopycnal at the surface), vertical adaptation cannot increase the horizontal resolution but can help better to resolve the front by moving more calculation points to the surface at the lower density side and more points to the deeper part on the dense side of the front. The vertical grid adaptation then has to ensure some lateral regularity of the grid in order not to allow too fast grid changes, otherwise larger truncation errors or problems similar to the internal pressure gradient error must be expected. The implementation of such extended grid adaptation methods will be discussed in a follow-up paper.

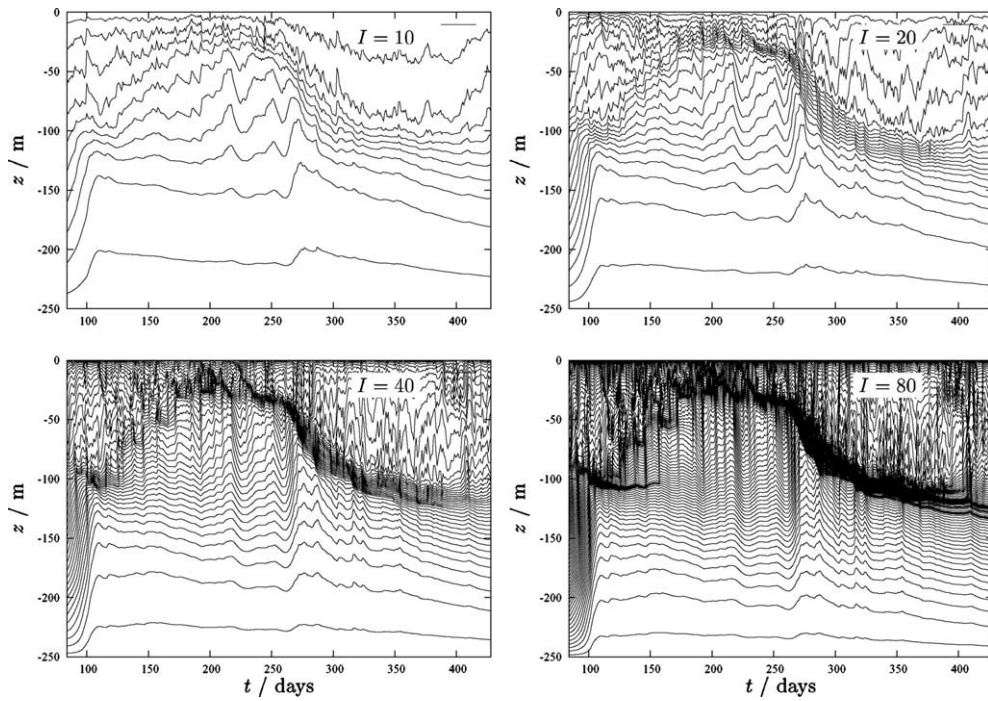


Fig. 22. Open ocean mixed layer experiment: adaptive grids for 10, 20, 40 and 80 layers which have been computed by means of method 3.

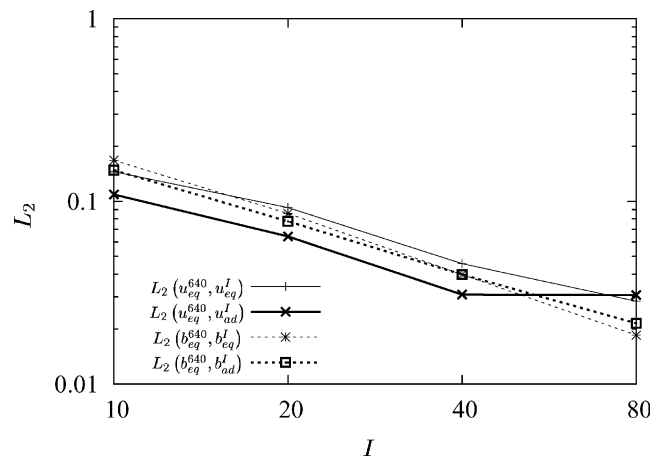


Fig. 23. Open ocean mixed layer experiment: integral rms errors between results for four resolutions for the adaptive grid (method 3) and the equidistant grid, both in relation to the high resolution ($I = 640$) equidistant solution.

Acknowledgements

The work of Hans Burchard is partially funded by the Alexander von Humboldt prize awarded by the National Fund for Scientific Research of Belgium for the academic year 2002/2003. Jean-

Marie Beckers is a Research Associate with the National Fund for Scientific Research of Belgium. The European project SOFT (EVK3-CT-2000-00028) allowed the performance of this work. The National Fund for Scientific Research, Belgium is acknowledged for the financing of a super-computer. The numerical calculations for this publication have been carried out by means of the Public Domain General Ocean Turbulence Model (GOTM, <http://www.gotm.net>). We are grateful to two anonymous reviewers for their constructive comments on our manuscript. This is MARE publication 008.

References

- Axell, L., Liungman, O., 2001. A one-equation turbulence model for geophysical applications: comparison with data and the k -epsilon model. *Environ. Fluid Mech.* 1, 71–106.
- Beckers, J.-M., 1991. Application of a 3D model to the Western Mediterranean. *J. Mar. Sys.* 1, 315–332.
- Beckers, J.-M., Burchard, H., Deleersnijder, E., Mathieu, P.-P., 2000. Numerical discretisation of rotated diffusion operators in ocean models. *Monthly Weather Rev.* 128, 2711–2733.
- Beckmann, A., Döscher, R., 1997. A method for improved representation of dense water spreading over topography in geopotential-coordinate models. *J. Phys. Oceanogr.* 27, 581–591.
- Bleck, R., 2002. An oceanic general circulation model framed in hybrid isopycnic-cartesian coordinates. *Ocean Modelling* 4, 55–88.
- Bleck, R., Rooth, C., Hu, D., Smith, L., 1992. Salinity-driven thermocline transients in a wind-and thermohaline-forced isopycnic coordinate model of the North Atlantic. *J. Phys. Oceanogr.* 22, 1486–1505.
- Blumberg, A.F., Mellor, G.L., 1987. A description of a three dimensional coastal ocean model. In: Heaps, N. (Ed.), *Three dimensional Shelf Models*. In: *Coastal Estuarine Sci.*, vol. 5. AGU, Washington, BC, pp. 1–16.
- Brockmann, U.H., Eberlein, K., Huber, K., Neubert, H.-J., Radach, G., Schulze, L. (Eds.), *JONSDAP '76: FLEX/INOUT Atlas, ICES Oceanographic Data Lists and Inventories*, vol. 1 (63), Conseil International pour l'Exploration de la Mer, Copenhagen, Denmark, 1984.
- Bryan, K., 1969. A numerical method for the study of the circulation of the world ocean. *J. Comput. Phys.* 4, 347–376.
- Burchard, H., Baumert, H., 1995. On the performance of a mixed-layer model based on the k - ϵ turbulence closure. *J. Geophys. Res.* 100, 8523–8540.
- Burchard, H., Bolding, K., 2001. Comparative analysis of four second-moment turbulence closure models for the oceanic mixed layer. *J. Phys. Oceanogr.* 31, 1943–1968.
- Burchard, H., Bolding, K., 2002. GETM—a general estuarine transport model. Scientific documentation, Tech. Rep. EUR 20253 EN, European Commission.
- Burchard, H., Deleersnijder, E., 2001. Stability of algebraic non-equilibrium second-order closure models. *Ocean Modelling* 3, 33–50.
- Burchard, H., Petersen, O., 1997. Hybridisation between σ and z coordinates for improving the internal pressure gradient calculation in marine models with steep bottom slopes. *Int. J. Numer. Meth. Fluids* 25, 1003–1023.
- Burchard, H., Petersen, O., 1999. Models of turbulence in the marine environment—A comparative study of two-equation turbulence models. *J. Mar. Sys.* 21, 29–53.
- Burchard, H., Petersen, O., Rippeth, T.P., 1998. Comparing the performance of the Mellor–Yamada and the k - ϵ two-equation turbulence models. *J. Geophys. Res.* 103, 10,543–10,554.
- Burchard, H., Bolding, K., Villarreal, M.R., 1999. GOTM—a general ocean turbulence model. Theory, applications and test cases, Tech. Rep. EUR 18745 EN, European Commission.
- Canuto, V.M., Howard, A., Cheng, Y., Dubovikov, M.S., 2001. Ocean turbulence. Part I: One-point closure model. Momentum and heat vertical diffusivities. *J. Phys. Oceanogr.* 31, 1413–1426.
- D'Alessio, S.D.J., Abdella, K., McFarlane, N.A., 1998. A new second-order turbulence closure scheme for modeling the oceanic mixed layer. *J. Phys. Oceanogr.* 28, 1624–1641.
- de Kok, J.M., 1992. A 3D finite difference model for the computation of near- and far-field transport of suspended matter near a river mouth. *Cont. Shelf Res.* 12, 625–642.

- Deleersnijder, E., Luyten, P., 1994. On the practical advantages of the quasi-equilibrium version of the Mellor and Yamada level 2.5 turbulence closure applied to marine modelling. *Appl. Math. Modelling* 18, 281–287.
- Deleersnijder, E., Ruddick, K.G., 1992. A generalized vertical coordinate for 3D marine problems. *Bulletin de la Societe Royale des Sciences de Liege* 61, 489–502.
- Denman, K.L., 1973. A time-dependent model of the upper ocean. *J. Phys. Oceanogr.* 3, 173–184.
- Dewar, W., McDougall, T., 2000. The numerical solution of the one-dimensional advection–diffusion equation in layered coordinates. *Monthly Weather Rev.* 128, 2575–2587.
- Fiedler, B., 2002. Grid adaptation and its effect on entrainment in an E–I model of the atmospheric boundary layer. *Monthly Weather Rev.* 130, 733–740.
- Freeman, N.G., Hale, A.M., Danard, M.B., 1992. A modified sigma equations’ approach to the numerical modeling of Great Lakes hydrodynamics. *J. Geophys. Res.* 77, 1050–1060.
- Frey, H., 1991. A three-dimensional, baroclinic shelf sea circulation model. 1. The turbulence closure scheme and the one-dimensional test model. *Cont. Shelf Res.* 11, 365–395.
- Friedrich, H., 1983. Simulation of the thermal stratification at the FLEX central station with a one-dimensional integral model. In: Sündermann, J., Lenz, W. (Eds.), *North Sea Dynamics*. Springer, Berlin, pp. 396–411.
- Gaspar, P., Gregoris, Y., Lefevre, J., 1990. A simple eddy kinetic energy model for simulations of the oceanic vertical mixing: Tests at station Papa and long-term upper ocean study site. *J. Geophys. Res.* 95, 16179–16193.
- Gerdes, R., 1993. A primitive equation ocean circulation model using a general vertical coordinate transformation. 1. Description and testing of the model. *J. Geophys. Res.* 98, 14683–14701.
- Gill, A.E., 1982. *Atmosphere–Ocean Dynamics*, International Geophysics Series, vol. 30, Academic Press.
- Griffies, S., Böning, C., Bryan, F., Chassignet, E., Gerdes, R., Hasumi, H., Hirst, A., Treguier, A.-M., Webb, D., 2000. Developments in ocean climate modeling world climate research programme/world ocean circulation experiment working group on ocean model development. *Ocean Modelling* 2, 123–192.
- Haidvogel, D.B., Beckmann, A., 1999. In: *Numerical Ocean Circulation Modelling Series on Environmental Science and Management*, vol. 2. Imperial College Press, London.
- Holt, J., James, I., 2001. An s-coordinate density evolving model of the Northwest European continental shelf- 1, model description and density structure. *J. Geophys. Res.* 106, 14015–14034.
- Kantha, L.H., Clayson, C.A., 1994. An improved mixed layer model for geophysical applications. *J. Geophys. Res.* 99, 25235–25266.
- Kasahara, A., 1974. Various vertical coordinate systems used for numerical weather predictions. *Monthly Weather Rev.* 102, 509–522.
- Kato, H., Phillips, O.M., 1969. On the penetration of a turbulent layer into stratified fluid. *J. Fluid Mech.* 37, 643–655.
- Lander, J.W.M., Blokland, P.A., de Kok, J.M., 1994. The three-dimensional shallow water model TRIWAQ with a flexible vertical grid definition, Tech. Rep. RIKZ/OS-96.104x, SIMON A report 96-01, National Institute for Coastal and Marine Management/RIKZ, The Hague, The Netherlands.
- Large, W.G., McWilliams, J.C., Doney, S.C., 1994. Oceanic vertical mixing: a review and a model with nonlocal boundary layer parameterisation. *Rev. Geophys.* 32, 363–403.
- Leonard, B.P., 1991. The ULTIMATE conservative difference scheme applied to unsteady one-dimensional advection. *Comput. Meth. Appl. Mech. Eng.* 88, 17–74.
- Liseikin, V., 1999. *Grid Generation Methods*. Springer, Berlin-Heidelberg.
- Madec, G., Delecluse, P., Imbard, M., Levy, C., 1998. Opa 8.1 ocean general circulation model reference manual 11, 1–91.
- Martin, P.J., 1985. Simulation of the mixed layer at OWS November and Papa with several models. *J. Geophys. Res.* 90, 903–916.
- Mellor, G.L., 2001. One-dimensional, ocean surface layer modeling, a problem and a solution. *J. Phys. Oceanogr.* 31, 790–803.
- Mironov, D.V., Gryanik, V.M., Moeng, C.-H., Olbers, D.J., Warncke, T.H., 2001. Vertical turbulence structure and second-moment budgets in convection with rotation: a large-Eddy Simulation study. *Quart. J. Royal Meteorol. Soc.* 126, 477–515.
- Patankar, S.V., 1980. *Numerical Heat Transfer and Fluid Flow*. McGraw-Hill, New York.
- Pietrzak, J., 1998. The use of TVD limiters for forward-in-time upstream-biased advection schemes in ocean modeling. *Monthly Weather Rev.* 126, 812–830.

- Pietrzak, J., Jakobson, J., Burchard, H., Vested, H.-J., Petersen, O., 2002. A three-dimensional hydrostatic model for coastal and ocean modelling using a generalised topography following co-ordinate system. *Ocean Modelling* 4, 173–205.
- Pohlmann, T., 1997. Estimating the influence of advection during FLEX'76 by means of a three-dimensional shelf sea circulation model. *Dt. Hydrogr. Z.* 49, 215–226.
- Price, J.F., 1979. On the scaling of stress-driven entrainment experiments. *J. Fluid Mech.* 90, 509–529.
- Roe, P.L., 1985. Some contributions to the modeling of discontinuous flows. *Lect. Notes Appl. Math.* 22, 163–193.
- Simpson, J.H., Burchard, H., Fisher, N.R., Rippeth, T.P., 2002. Modelling the cycle of tidal dissipation in a region of tidal straining. *Cont. Shelf Res.* 22, 1615–1628.
- Soetje, K.C., Huber, K., 1980. A compilation of data on the thermal stratification at the central station in the northern North Sea during FLEX'76. "Meteor"-Forsch.-Ergebnisse, Reihe A 22, 69–77.
- Song, Y., Haidvogel, D.B., 1994. A semi-implicit ocean circulation model using a generalised topography-following coordinate. *J. Computat. Phys.* 115, 228–244.
- Stanev, E., Beckers, J.-M., 1999. Barotropic and baroclinic oscillations in strongly stratified ocean basins. Numerical study of the Black Sea. *J. Mar. Sys.* 19, 65–112.
- Thompson, J., Warsi, Z., Mastin, C., 1985. *Numerical grid generation—foundations and applications*. Elsevier, New-York.
- van Leer, B., 1979. Toward the ultimate conservative difference scheme. V: A second order sequel to Godunov's method. *J. Computat. Phys.* 32, 101–136.
- Villarreal, M.R., 2000. Parameterisation of turbulence in the ocean and application of a 3D baroclinic model to the Ria de Pontevedra. Ph.D. thesis, Departamento de Fisica da Materia Condensada, Grupo de Fisica Non-Lineal, Universidade de Santiago de Compostela, 2000, available from the World Wide Web at <http://www.gotm.net>.
- Willis, G.E., Deardorff, J.W., 1974. A laboratory model of the unstable planetary boundary layer. *J. Atmos. Sci.* 31, 1297–1307.